physica status solidi b
www.pss-b.com

Hole Spin Coherence in InAs/InAlGaAs Self-Assembled Quantum Dots Emitting at Telecom Wavelengths

Eiko Evers, Nataliia E. Kopteva, Vitalie Nedelea, Andrei Kors, Ranbir Kaur, Johann Peter Reithmaier, Mohamed Benyoucef, Manfred Bayer, and Alex Greilich**

Measurements of the longitudinal and transverse spin relaxation times of holes in an ensemble of vertically tunnel-coupled self-assembled InAs/$In_{0.53}Al_{0.24}Ga_{0.23}As$ quantum dots (QDs), emitting in the telecom spectral range, are reported. The spin coherence is determined using the spin mode-locking method in the inhomogeneous ensemble of QDs. Modeling the signal allows us to extract the hole spin coherence time to be in the range of $T_2 = 0.02 - 0.4\,\mu s$. The longitudinal spin relaxation time $T_1 = 0.5\,\mu s$ is measured using the spin inertia method. The parameters investigated allow us to suggest that the main relaxation mechanism at low magnetic fields is related to the electron–hole spin exchange.

1. Introduction

Quantum repeaters (QRs) are critical for achieving end-to-end security in fiber optics-based quantum communication networks.[1] They allow the entanglement of fiber optic sections through quantum mechanical coupling or quantum teleportation, eliminating the need for additional security measures at the nodes.[2,3]

Implementing QRs requires quantum storage devices with sufficiently long coherence times to enable the stored state's entanglement with a photon for subsequent transmission.[4,5] For this purpose, semiconductor quantum dots (QDs) seem to be an attractive candidate. Entanglement of a carrier spin with an emitted photon was demonstrated in QDs,[6,7] as well as an entanglement operation of two remote spins induced by a measurement of two indistinguishable photons.[8] The listed investigations focused mostly on the near-infrared QDs with an optical excitation wavelength of ≈0.9 μm. However, to be of practical relevance for fiber optics networks, QDs must operate in the C-telecom band, around 1.55 μm.

Recent years have witnessed substantial advancements in single photon emission[9–15] and coherent manipulation of spin states for QDs operating in the telecom wavelength range.[16–18] While it has been established that spins can be efficiently oriented and manipulated through optical pulses, a critical aspect, the spin coherence time, representing the relevant information lifetime, has remained unexplored and insufficiently represented. Ref. [19] demonstrates studies of undoped and n-doped QDs in the telecom range with no indications of the resident carrier, which led to a radiatively limited time scale of spin relaxation below 1 ns. Further advances were presented in ref. [20], where the appearance of resident electrons allowed the authors to measure the limiting factors of electron spin coherence, while no spin mode-locking (SML) was observed.

This article extends the research to resident hole spins, which can be superior to electron spins due to a weaker coupling to nuclear surroundings. Furthermore, we present the appearance of the SML effect for holes at the telecom spectral range, which allows us to extract the hole spin coherence while measuring an inhomogeneous ensemble of spins.[21,22]

2. Experimental Section

The investigated QD sample is grown by molecular-beam epitaxy on a (100)-oriented InP substrate. It consists of 5.5 nm InAs monolayers separated by $In_{0.53}Al_{0.24}Ga_{0.23}As$ barriers. The quaternary barrier serves multiple purposes: increasing the barrier height for the QDs and providing a waveguiding effect. The composition and morphology of the QD of similar structures can be found in ref. [23].

The sample schematic is presented in **Figure 1**a. The bottom barrier contains a Si δ-doped layer with the doping density of $10^{10}\,cm^{-2}$ at a distance of 15 nm from the bottom QD layer to provide resident electrons in the QDs. The density of QDs is $\approx 10^{10}\,cm^{-2}$. We use eight QD layers (to increase signal) separated by a barrier of 15 nm to additionally study the implications of carriers tunneling between the neighboring QDs. While the separation of 15 nm between the QD layers is used for growth, the QDs themselves have a height of about

E. Evers, N. E. Kopteva, V. Nedelea, M. Bayer, A. Greilich
Experimentelle Physik 2
Technische Universität Dortmund
44221 Dortmund, Germany
E-mail: alex.greilich@tu-dortmund.de

A. Kors, R. Kaur, J. Peter Reithmaier, M. Benyoucef
Institute of Nanostructure Technologies and Analytics (INA)
CINSaT
University of Kassel
D-34132 Kassel, Germany
E-mail: m.benyoucef@physik.uni-kassel.de

The ORCID identification number(s) for the author(s) of this article can be found under https://doi.org/10.1002/pssb.202400174.

DOI: 10.1002/pssb.202400174

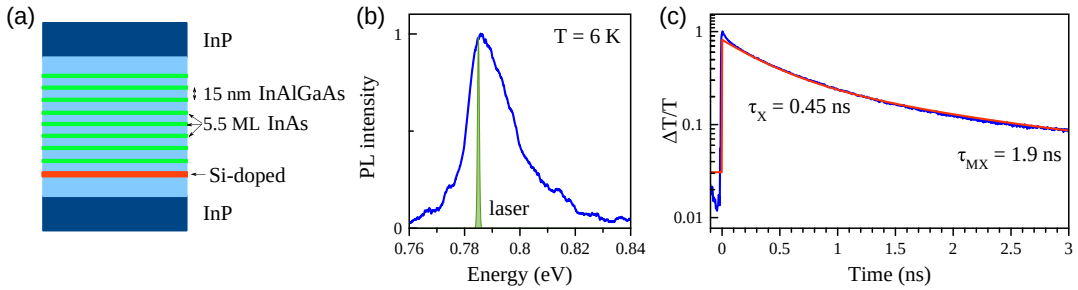

Figure 1. a) Schematic of the sample structure: green represents the InAs layers of QDs, surrounded by 15 nm barriers of $In_{0.53}Al_{0.24}Ga_{0.23}As$. Red is the Si δ-doped layer. b) PL spectrum measured at $T = 6$ K. The green line is the spectrum of the laser at 0.785 eV with full width at half maximum of 0.8 meV. c) Dynamics of differential transmission ($\Delta T/T$) excited and detected at the energy of $E_p = 0.784$ eV (blue). The red line is fit by a two exponential decay with $\tau_X = 0.45$ ns and $\tau_{MX} = 1.9$ ns. Pump and probe powers are 17 and 1 mW, respectively.

9–13 nm,[19] which makes the distance between the vertically stacked QDs correspondingly smaller.

The sample is placed in helium gas for measurements at $T = 6 - 60$ K. Figure 1b shows the photoluminescence (PL) spectrum of the QD ensemble measured at $T = 6$ K. The PL spectrum has its maximum at around 0.784 eV and shows inhomogeneously broadened emission with a width of about 20 meV due to the spread of QD parameters. Magnetic fields up to 4 T are applied either transverse to the k-wavevector of light (Voigt geometry, B_V) or longitudinally to this direction (Faraday geometry, B_F).

The spin coherence of spin-polarized carriers is measured by pump–probe Faraday rotation (FR).[24] To excite the QDs with telecom wavelengths, we use a pulsed Ti:sapphire laser pumping an optical parametric oscillator at a pulse repetition rate of 76.7 MHz (pulse repetition period of $T_R = 13$ ns). The spectral width of the laser is below 2 nm (0.8 meV) with a pulse duration of about 1.5 ps and is shown by the green spectrum in the Figure 1b. The laser beam is split into the pump and probe, which are focused on the sample with the spot diameter of 120 µm for the pump and 100 µm for the probe. The photon energies (E_p) of both pulses are the same.

Using the probe laser spot diameter of 100 µm, with the QDs density of 10^{10} cm^{-2} = 100 µm^{-2}, and taking the spectral width of the laser (0.8 meV) and the PL width of the QDs (20 meV) into account, we calculate the number of excited QDs to be 3.1×10^4 per single layer. All the experiments are done in the transmission geometry where we excite QDs in all eight layers, so the total amount of the tested QDs is about 2.5×10^5 in all pump–probe experiments. We do not take any reflections at the material interfaces into account. The number of QDs participating in nonresonant PL measurements is about 6.3×10^6. Here, we consider that the laser spot size is similar, and all QD layers are excited.

The circularly polarized pump pulses create the spin polarization, while the linearly polarized probe pulses detect the spin polarization via the Faraday rotation effect. To suppress the scattered light, we use a double-modulation technique. The pump beam is modulated between σ^+ and σ^- by an electro-optical modulator at $f_m = 10$ kHz. The probe beam is intensity modulated by a photoelastic modulator at 100 kHz. The signal is amplified by a lock-in device operated at a differential frequency and recorded versus the time delay between the pump and probe.

3. Experimental Results and Discussion

3.1. Spin Signal Components

Figure 1c shows the exciton population recombination dynamics measured by differential transmission ($\Delta T/T$) at the PL maximum $E_p = 0.784$ eV. Linearly polarized pump pulses generate the exciton population, and its dynamics are monitored by the probe with orthogonal linear polarization. The $\Delta T/T$ is best fitted by two exponential decay functions, giving the short decay time of $\tau_X = 0.45$ ns and the long decay time of $\tau_{MX} = 1.9$ ns. The short decay component is in the time range of the direct excitonic recombination time, as was previously seen on very similar single-layer QD structure.[25] As the excitation and detection are done resonantly in our case, we expect a signal only from a subensemble of QDs close to the laser energy. In principle, it is possible to have two types of QDs with different relaxation times at the same optical energy. However, including all results presented in the article, like nonoscillating decay at applied magnetic fields, we conclude that the only plausible explanation for the long-time component (1.9 ns) is that it is related to the proximity with other QDs and, therefore, to tunneling processes leading to a possibility of the creation of indirect excitonic or molecular states. The (maximum) barrier thickness of 15 nm is considered thin enough for electrons to tunnel between the QDs.[26]

An exemplary Faraday rotation signal from the QD ensemble at $B_V = 0.2$ T is shown in **Figure 2**a by the blue trace. We decompose it into three components, as shown by the colored traces below, using the following fit function

$$S = \sum_i A_i \cos(\omega_i t) \exp(-t^2/2T_{2,i}^{*2}) \quad (1)$$

The Gaussian type of decay is governed by the spectral shape of the laser and the ensemble inhomogeneity of QDs. Here, the index i gives the component number, $\omega_i = \mu_B g_i B_V/\hbar$ is the corresponding Larmor precession frequency, and g_i is the associated g-factor. μ_B is the Bohr magneton, and $\hbar$ is the reduced Planck constant. $T_{2,i}^*$ is the spin dephasing time.

The dependencies of the Larmor frequencies of electrons and holes on the transverse magnetic field (B_V) are linear, with the slopes being proportional to their g-factors. We obtain for the electron $|g_e| = 1.88$ and for the hole $|g_h| = 0.60$. These values

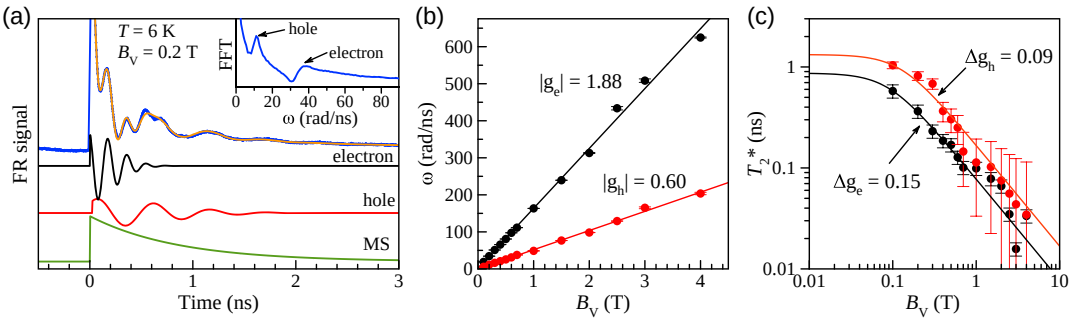

Figure 2. a) Faraday rotation signal for $B_V = 0.2$ T, $T = 6$ K, and $E_p = 0.785$ eV shown by blue trace. The pump and probe powers are 15 and 1 mW, respectively. The black and red traces are the electron and the hole spin contributions, respectively. The green trace is the signal of the molecular states. The orange curve is the sum of all contributions. The inset shows the fast Fourier transform of the blue trace. b) The Larmor precession frequencies of electron (black) and hole (red) versus the transverse magnetic field (B_V). Linear fits give $|g_e| = 1.88$ and $|g_h| = 0.60$. c) Dephasing times (T_2^*) of electron (black) and hole (red) as functions of B_V. The data are fitted using Equation (2).

agree with the data from refs. [19,25], where the assignment of the two contributions to electron and hole is done based on the differences in their *g*-factor anisotropies in magnetic field and corresponding theoretical calculations.

The spin dephasing times (T_2^*) of electrons and holes strongly depend on B_V as shown in Figure 2c. At magnetic fields above 0.1 T, the spin dephasing is governed by the spread of the *g*-factor values, which is related to the inhomogeneities in the ensemble of QDs. At low magnetic fields, the spin dephasing saturates at the values determined by the hyperfine interaction with the fluctuating nuclear spin environment. As shown in Figure 2c, the hole spin dephasing saturates at a higher value of $T_{2,h}^* = 1.0$ ns than the electron with $T_{2,e}^* = 0.6$ ns. This can be explained by the weaker hyperfine coupling of the hole.[27] Our estimation of the electrons' spin dephasing time using the equation provided by Merkulov et al.[28] is $T_{2,e}^* = 0.55$ ns, which is very close to the value of 0.6 ns obtained in our measurements. Considering that the hyperfine interaction of hole spins is an order of magnitude weaker, one expects the dephasing time to be an order of magnitude longer. The observed difference suggests that one should consider an additional dephasing mechanism, which we provide in the discussion part of the article.

The dependence of T_2^* on B_V can, therefore, be described by

$$T_{2,i}^* = \hbar / \sqrt{(\Delta g_i \mu_B B_V)^2 + (g_i \mu_B \Delta B_i)^2} \quad (2)$$

where the index i gives the electron or hole contribution, Δg_i is the spread of *g*-factors, and ΔB_i is the limiting factor at low fields.[20] The fitting curves for electron and hole are shown in Figure 2c by the solid lines. The evaluation gives $\Delta g_e = 0.15$, $\Delta g_h = 0.09$, and $\Delta B_e = 7$ mT, $\Delta B_h = 13$ mT. The reported *g*-factor dispersions exceed the previously reported $\Delta g_e = 0.002$, $\Delta g_h = 0.05$ for InAs/$In_{0.53}Al_{0.24}Ga_{0.23}As$ QDs.[25] The sample under study has a small distance between the QD layers, which leads to the possibility of tunneling between the QDs for the electrons. It is known that the value of the *g*-factor depends strongly on the mixing of the barrier, as it is different in the barrier material.[29] Holes, in contrast, have a reduced probability of tunneling due to their higher effective mass. As a consequence, electrons are much more sensitive to the potential variations and should have a higher spread of *g*-factor values, as is observed in our experiment. The similarity of the hole's spread of *g*-factors to the previous report with decoupled QDs supports our assumption of a localized nature of the holes in our sample.

The spread of the parameters in the ensemble of QDs manifests itself in the broadening of the PL line. Despite that, the electron and hole *g*-factors show a systematic variation throughout the range of optical transition energies in the ensemble, as was earlier observed for near-infrared QDs and telecom range QDs.[25] Using the spectrally narrow laser, one can select and test QD subensembles by tuning the central energy E_p. The dependence of $|g_h|$ on the pump–probe energy is presented in **Figure 3**a, with the absolute value increasing with E_p, as shown by the red dots. The dependence can be described by the linear function $|g_h| = AE_p - B$, with $A = 2 \times 10^{-3}$ meV^{-1} and $B = 1 \times 10^{-3}$. The electron *g*-factor $|g_e|$ shows the opposite tendency: the absolute value is decreasing with E_p, as shown in Figure 3b. It can be described by $|g_e| = -AE_p + B$, with $A = 7.3 \times 10^{-3}$ meV^{-1} and $B = 7.7 \times 10^{-3}$. The electron *g*-factor is expected to be negative. This observation is consistent with previous studies on (In,Ga)As QDs[30,31] and aligns with the Roth–Lax–Zwerdling relation for bulk semiconductors.[25,32]

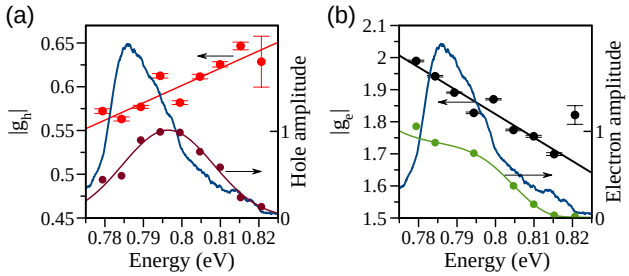

Figure 3. a) Red dots present the dependence of $|g_h|$ on the central laser energy E_p. The red line is a linear fit to the data. The brown dots show the spectral dependence of the normalized hole spin amplitude contribution to the FR signal. The solid line is a guide for the eye. b) Black dots present the dependence of $|g_e|$ on E_p. The black solid line is a linear fit. The green dots show the spectral dependence of the normalized electron contribution. The solid line is a guide for the eye. The blue line is the PL.

If we now compare the amplitude of the signal contributions, one can see that the amplitude of the Faraday rotation signal for the hole has a pronounced resonance with the maximum at $E_p = 0.796$ eV (see Figure 3a). By contrast, the electron amplitude constantly increases toward the low-energy side of PL, as shown in Figure 3b.

The observed increase of the electron-related spin component at the lower energy indicates that more QDs contain an electron at lower energies. This experimental fact can be interpreted in terms of electron doping and a tunneling processes. It is known that for MBE-grown QDs, each upper layer of the coupled QDs contains bigger QDs, which correspondingly have a lower optical transition energy. Therefore, there is an increased probability for electrons to tunnel toward (or populate) QDs in the lower energy tail of the PL and shift the expected amplitude maximum. We concentrate on the spectral position with the highest hole spin amplitude for further measurements.

Finally, Figure 2a demonstrates an additional, nonoscillating decaying signal component (MS), despite the applied external magnetic field. Usually, a nondecaying signal is observed under a tilted magnetic field (we rule this possibility out) or in the case of a tilted spin quantization axis.[33] This property requires further investigations, including studies of the influence of the barrier thickness and the type of resident charging. We leave this issue for future studies and focus on the signal from the carriers localized in a QD, similar to isolated QDs.

3.2. Longitudinal Spin Relaxation

To measure the longitudinal spin lifetime (T_s) and the spin relaxation time (T_1) of the holes, we employ the spin inertia technique.[34] The helicity of the pump is modulated between σ^+ and σ^- with the frequency f_m. When the modulation period becomes shorter than the spin lifetime T_s, the averaged signal amplitude starts to decrease. The measurement of spin lifetimes is done at negative relative time delays with probe testing the system 50 ps before the pump arrival. A longitudinal magnetic field ($B_F = 4.6$ mT), larger than the observed nuclear field fluctuations, is applied to decouple the hole spins from the fluctuating nuclear spin environment.

Figure 4a shows the measured polarization recovery curve with the sweeping of the longitudinal magnetic field while measuring the Faraday rotation signal at −50 ps delay, just before the pump-pulse arrival. The form of the polarization recovery curve is nontrivial and has an M-shape. The origin of such appearance was thoroughly studied in our previous publications.[35,36] The narrow dip at zero field, with a half width at half maximum (HWHM) of about 1 mT is proportional to nuclear field fluctuations seen by the hole spins, and a broader inverted peak (HWHM of 18 mT) is related to the relaxation of the electrons in a trion state interacting with the fluctuating nuclear environment. The spin polarization reaches a maximum at fields above 2.5 mT for the hole spin component and saturates as the nuclear spin fluctuations are suppressed. Therefore, for the fields above 4.6 mT, no change in T_1 time is expected. Note that both carriers have a g-factor anisotropy, which leads to the difference in the nuclear field fluctuations measured in transverse and longitudinal directions.

The spin inertia curves are shown in Figure 4b at $B_F = 4.6$ mT for different pump powers. The decay of the FR signal in dependence on f_m can be described by

$$S(f_m) = S_0/\sqrt{1 + (2\pi f_m T_s)^2} \tag{3}$$

with $T_s = 0.3$ µs at the pump power of 14 mW. The extrapolation of T_s dependence on power to zero gives the spin relaxation time $T_1 = 0.5$ µs (see Figure 4c). The experimental data can be well fitted by this form, indicating spin relaxation times exceeding the laser repetition period. This allows us to attribute this signal to resident carrier spins.

The temperature dependence of T_1 is shown in Figure 4d and is commonly governed by two processes. At low temperatures (<10 K) and at a magnetic field lower than the nuclear spin fluctuations (<30 mT), the spin relaxation time is limited by the interactions with the nuclear spin fluctuations. At higher temperatures (>10 K), longitudinal phonons are activated, accelerating the spin relaxation. The theoretical description accounting for the nuclear spin fluctuations and longitudinal optical phonons is discussed in refs. [37,38]. At temperatures above 50 K, the error of the measured signal becomes large, and the data are unreliable.

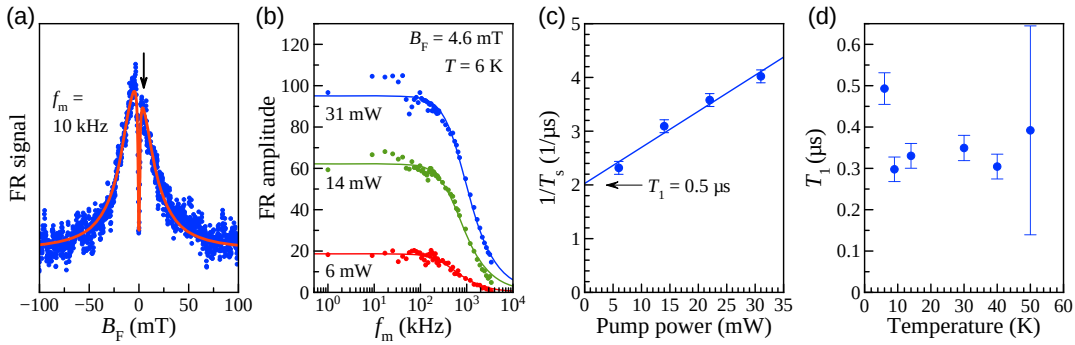

Figure 4. a) Polarization recovery curve measured for $f_m = 10$ kHz. Pump power 1.2 mW; probe power 0.5 mW. The arrow shows the position for measurements presented in panel (b). b) Faraday rotation amplitude (dots) at the pump–probe delay of −50 ps as a function of the pump modulation frequency f_m measured in a longitudinal magnetic field of $B_F = 4.6$ mT for different pump powers. $E_p = 0.784$ eV. The lines are fitted according to Equation (3) describing the spin inertia effect. c) Pump power dependence of inverse spin lifetimes $1/T_s$. A linear extrapolation to zero power gives the intrinsic spin relaxation time $T_1 = 0.5$ µs. d) T_1 dependence on temperature.

In the discussion part, we thoroughly discuss the possible relaxation mechanism, including the temperature dependence.

3.3. Transverse Spin Relaxation

The large spread of g-factors and long spin relaxation times are promising conditions for the SML effect, observed on electrons in n-doped (In,Ga)As/GaAs QDs,[39,40] on holes in p-doped InAs/GaAs QDs,[21,22] and recently on holes in $CsPb(Cl,Br)_3$ perovskite nanocrystals.[41] In this article, we show the SML effect for the holes in the QDs ensemble emitting in the telecom range.

The resident hole spin polarization is created through the trion excitation mechanism in the pump–probe Faraday rotation.[24] The polarized spins precess about B_V and loose their polarization with the spin coherence time of a single carrier T_2. After the action of an infinite number of pulses with a repetition period of T_R, the spin polarization accumulates for carriers with $T_2 > T_R$. In the inhomogeneous ensemble of QDs, the sum of the multiple oscillating signals with Larmor frequencies commensurate with ω_R contributes to the SML signal. It manifests itself in the revival of the FR signal at negative delays (probe arrives before pump). Such a signal is shown in the inset of **Figure 5**a. To assign the carrier contribution to it, we measure the SML dependence on B_V. From the g-factor values, we conclude that the signal is related to the hole spins.

To evaluate the spin coherence time T_2, we have decomposed the signal into its components. Figure 5b demonstrates the remaining signal component after subtraction of the nonoscillating decaying component, the electron signal, and the hole signal with short dephasing times at positive time delays. The signal decay time at negative and positive delay times is given by the spin dephasing time T_2^*, which is limited by the spread of g-factors, as discussed in Section 3.3.1. The relation of the signal amplitude before the pump pulse arrival S_b to the amplitude after the pulse action S_a is determined by T_2 and the pump power, and allows one to extract the corresponding time.

To estimate the T_2, we use the model developed in refs. [24,42]. Each optical pulse changes the spin polarization proportional to pump pulse area Θ (or the pump power in the experiment)

$$S_{z,a} = -\frac{\sin^2(\Theta/2)}{4} + \frac{\cos^2(\Theta/2)+1}{2} S_{z,b} \tag{4}$$

$$S_{y,a} = \cos(\Theta/2) S_{y,b} \tag{5}$$

$$S_{x,a} = \cos(\Theta/2) S_{x,b} \tag{6}$$

Here, the z-component is directed along the k-wavevector of light, and the x-component is along B_V. Equations (4)–(6) assume rectangular optical pulses and do not include the optical detuning of the laser energy from the trion resonance.

The dynamics of the hole spin polarization after optical excitation is determined by the Bloch equations

$$S_z(t) = [S_{z,a}\cos(\omega t) + S_{y,a}\sin(\omega t)]\exp(-t/T_2) \tag{7}$$

$$S_y(t) = [S_{y,a}\cos(\omega t) - S_{z,a}\sin(\omega t)]\exp(-t/T_2) \tag{8}$$

$$S_x(t) = S_{x,a}\exp(-t/T_1) \tag{9}$$

Note that the S_x component cannot be created without optically detuned optical pulses. We consider the spin relaxation time anisotropy in the sample plane.

The accumulation of the spin polarization for an infinite number of optical pulse actions is calculated numerically for each individual spin in the ensemble. We use a Gaussian distribution of the g-factors in the ensemble with the width of $2\Delta g_h = 0.2$. The resulting amplitude relation S_b/S_a is determined by T_2 and Θ. For the calculations, we use the experimentally measured g_h, Δg_h, with the result shown in Figure 5b by the red line.

The parameter Θ cannot be precisely evaluated from the experiment because the SML amplitude neither shows amplitude saturation nor Rabi oscillations in dependence on the pump power due to the high inhomogeneity of the QD ensemble. We, therefore, have to consider the range of pulse areas with $\Theta = 0.6\,\pi$, leading to the maximal $T_2 = 400$ ns, and the $\Theta = \pi$ with the minimal possible $T_2 = 20$ ns, both of which lead to the observed amplitude relation S_b/S_a.

4. Discussion

Previous studies have examined spin–orbit interaction, which involves transitions between different spin levels facilitated by phonons and their effect on the T_1 time. For instance, single-phonon scattering mediated by spin–orbit interactions was employed to explain the relaxation of hole spins in (In,Ga)As QDs, resulting in T_1 times up to 270 µs at $B = 1.5$ T at

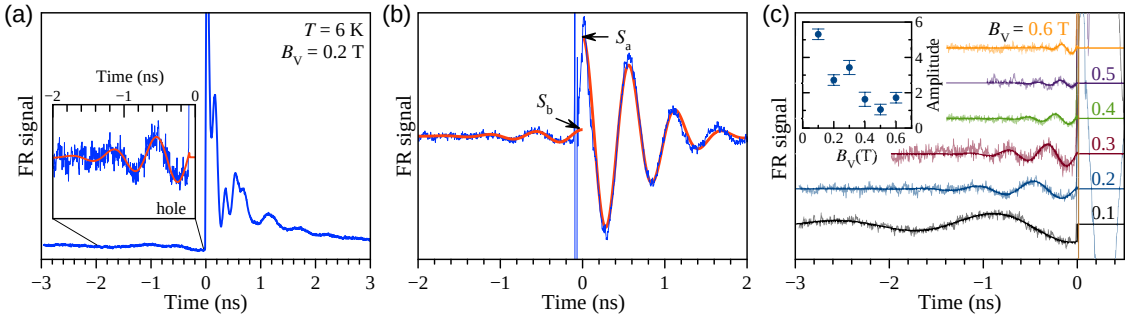

Figure 5. a) Faraday rotation signal measured at $B_V = 0.2$ T, $T = 6$ K, and $E_p = 0.785$ eV. The pump and probe powers are 15 and 1 mW. The inset shows the zoomed-in signal at negative time delays. b) The blue trace is the SML signal of the holes, and the red solid line shows its modeling. c) Magnetic field dependence of the negative time mode-locking signal with the corresponding fits. Insert shows the extracted fit amplitude.

$T = 8$ K.[43] Additionally, two-phonon-assisted spin relaxation was theoretically considered for hole spins, leading to T_1 times on the order of hundreds of microseconds at magnetic fields $B < 2$ T and temperatures of $T = 2$ K.[38,44] At low magnetic fields, as used for T_1 measurements in our case, the Zeeman splitting is small. The density of phonons that can match the Zeeman energy is decreased, and the single-phonon scattering mechanism becomes negligible.[37,45,46] Phonon-mediated hyperfine mechanisms have also been proposed, but the spin relaxation rate driven by the single-phonon-assisted process is zero without a magnetic field.[37]

The more recent ref. [47], studying near-infrared QDs demonstrates experimentally that T_1 is limited by two mechanisms: at low temperatures and low magnetic fields ($B < 2$ T), the hyperfine coupling with the nuclear spins of the host material limits the T_1 value close to 1 μs. Furthermore, the authors demonstrate the importance of the two-phonon-assisted mechanism for the hole spin relaxation, which leads to a quadratic dependence of the hole spin relaxation rate with temperature in the 7–50 K range, in good agreement with theoretical predictions.[37,38]

In our case, the observed T_1 is close to 0.3 μs and stays constant up to 50 K. Such behavior suggests that the two-phonon-assisted scattering is not the dominant mechanism, assuming similarity of the processes in near-infrared and telecom QDs. Additionally, no effects of nuclear-induced frequency focusing were observed in our work. Therefore, the hyperfine interaction is expected to be a less important factor for spin relaxation here.

When considering the T_2 spin relaxation at low magnetic fields, the effect of the nuclear fluctuations plays a major role at low temperatures ($T < 8$ K).[48] With the temperature increase, the mechanism of elastic scattering exploiting the broad phonon sidebands is expected to cause a rapid decrease in hole spin coherence.[49] The effect of the magnetic field on the hole spin coherence was shown to have a stabilizing effect for isolated QDs, with the T_2 time growing up to 4 μs at 2 T.[48] In our case, however, the observed mode-locking amplitude, and therefore, the hole spin coherence, decays in the magnetic field range of $0.1 - 0.6$ T, as shown in Figure 5c.

Considering the observed results, one can suggest an additional spin relaxation in the spirit of the Bir–Aronov–Pikus mechanism.[50] In our case, the localized hole spins interact with the weakly localized electrons that can tunnel between the dots.

The detected spin coherence is comparable with the one observed in InAs QDs emitting in the range of 0.9 μm, demonstrating $T_2 \approx 1$ μs.[48,51] However, to be useful for QR technology, we must reach spin coherence times close to milliseconds (100 km takes about 0.33 ms for light traveling). Such times could be achieved by using the coherence transfer to the nuclear surrounding in the QDs, showing coherence times in the required time range.[52,53] The feasibility of such protocol for semiconductor QDs is currently investigated by other groups[54,55] and recently a breakthrough in this direction was achieved for the strain-free GaAs QDs.[56] Taking into account that the strain-free environment might be very important for such coherence transfer, a new strain-free material for QDs emitting at telecom spectral range becomes important.[57]

5. Conclusions

Using the SML method, we could determine the range of the achievable spin coherence of holes, which exceeds previously measured values in similar types of QDs by at least an order of magnitude.[20] The hole spin lifetime of 0.5 μs is also extended and currently provides the upper limit for the hole spin coherence. However, the time is reduced compared to the hole spins localized in near-infrared QDs. Our conclusion for this type of sample is that the delocalized nature of electrons drives the relaxation of hole spins.

Acknowledgements

The authors acknowledge the financial support by the Deutsche Forschungsgemeinschaft in the frame of the ICRC TRR 160 (Project A1), DeLiCom, and DFG-Heisenberg grant-BE 5778/4-1. The authors also acknowledge the Bundesministerium für Bildung und Forschung in the frame of the project QR.X (contract nos. 16KISQ011 and 16KISQ005).

Open Access funding enabled and organized by Projekt DEAL.

Conflict of Interest

The authors declare no conflict of interest.

Data Availability Statement

The data that support the findings of this study are available from the corresponding author upon reasonable request.

Keywords

quantum dots, spin coherence, spin relaxation, telecom

Received: April 9, 2024
Revised: July 15, 2024
Published online: September 2, 2024

[1] H.-J. Briegel, W. Dür, J. I. Cirac, P. Zoller, *Phys. Rev. Lett.* **1998**, *81*, 5932.
[2] C.-W. Chou, J. Laurat, H. Deng, K. S. Choi, H. de Riedmatten, D. Felinto, H. J. Kimble, *Science* **2007**, *316*, 1316.
[3] Z.-S. Yuan, Y.-A. Chen, B. Zhao, S. Chen, J. Schmiedmayer, J.-W. Pan, *Nature* **2008**, *454*, 1098.
[4] M. K. Bhaskar, R. Riedinger, B. Machielse, D. S. Levonian, C. T. Nguyen, E. N. Knall, H. Park, D. Englund, M. Loncar, D. D. Sukachev, M. D. Lukin, *Nature* **2020**, *580*, 60.
[5] C. E. Bradley, S. W. de Bone, P. F. W. Möller, S. Baier, M. J. Degen, S. J. H. Loenen, H. P. Bartling, M. Markham, D. J. Twitchen, R. Hanson, D. Elkouss, T. H. Taminiau, *npj Quantum Inf.* **2022**, *8*, 122.
[6] W. B. Gao, P. Fallahi, E. Togan, J. Miguel-Sanchez, A. Imamoglu, *Nature* **2012**, *491*, 426.
[7] K. De Greve, L. Yu, P. L. McMahon, J. S. Pelc, C. M. Natarajan, N. Y. Kim, E. Abe, S. Maier, C. Schneider, M. Kamp, S. Höfling, R. H. Hadfield, A. Forchel, M. M. Fejer, Y. Yamamoto, *Nature* **2012**, *491*, 421.
[8] R. Stockill, M. J. Stanley, L. Huthmacher, E. Clarke, M. Hugues, A. J. Miller, C. Matthiesen, C. Le Gall, M. Atatüre, *Phys. Rev. Lett.* **2017**, *119*, 010503.

[9] M. Benyoucef, M. Yacob, J. P. Reithmaier, J. Kettler, P. Michler, *Appl. Phys. Lett.* **2013**, *103*, 162101.
[10] M. Paul, F. Olbrich, J. Höschele, S. Schreier, J. Kettler, S. L. Portalupi, M. Jetter, P. Michler, *Appl. Phys. Lett.* **2017**, *111*, 033102.
[11] F. Olbrich, J. Höschele, M. Müller, J. Kettler, S. Luca Portalupi, M. Paul, M. Jetter, P. Michler, *Appl. Phys. Lett.* **2017**, *111*, 133106.
[12] A. Musiał, P. Holewa, P. Wyborski, M. Syperek, A. Kors, J. P. Reithmaier, G. Sęk, M. Benyoucef, *Adv. Quantum Technol.* **2020**, *3*, 1900082.
[13] A. Musiał, M. Mikulicz, P. Mrowiński, A. Zielińska, P. Sitarek, P. Wyborski, M. Kuniej, J. P. Reithmaier, G. Sęk, M. Benyoucef, *Appl. Phys. Lett.* **2021**, *118*, 221101.
[14] B. Da Lio, C. Faurby, X. Zhou, M. L. Chan, R. Uppu, H. Thyrrestrup, S. Scholz, A. D. Wieck, A. Ludwig, P. Lodahl, L. Midolo, *Adv. Quantum Technol.* **2022**, *5*, 2200006.
[15] R. Katsumi, Y. Ota, T. Tajiri, S. Iwamoto, K. Ranbir, J. P. Reithmaier, M. Benyoucef, Y. Arakawa, *Appl. Phys. Express* **2022**, *16*, 012004.
[16] W. Rudno-Rudziński, M. Burakowski, J. P. Reithmaier, A. Musiał, M. Benyoucef, *Materials* **2021**, *14*, 4.
[17] P. Podemski, M. Gawelczyk, P. Wyborski, H. Salamon, M. Burakowski, A. Musial, J. P. Reithmaier, M. Benyoucef, G. Sęk, *Opt. Express* **2021**, *29*, 34024.
[18] L. Dusanowski, C. Nawrath, S. L. Portalupi, M. Jetter, T. Huber, S. Klembt, P. Michler, S. Höfling, *Nat. Commun.* **2022**, *13*, 748.
[19] V. V. Belykh, D. R. Yakovlev, J. J. Schindler, E. A. Zhukov, M. A. Semina, M. Yacob, J. P. Reithmaier, M. Benyoucef, M. Bayer, *Phys. Rev. B* **2016**, *93*, 125302.
[20] A. V. Mikhailov, V. V. Belykh, D. R. Yakovlev, P. S. Grigoryev, J. P. Reithmaier, M. Benyoucef, M. Bayer, *Phys. Rev. B* **2018**, *98*, 205306.
[21] F. Fras, B. Eble, B. Siarry, F. Bernardot, A. Miard, A. Lematre, C. Testelin, M. Chamarro, *Phys. Rev. B* **2012**, *86*, 161303.
[22] S. Varwig, A. Schwan, D. Barmscheid, C. Müller, A. Greilich, I. A. Yugova, D. R. Yakovlev, D. Reuter, A. D. Wieck, M. Bayer, *Phys. Rev. B* **2012**, *86*, 075321.
[23] C. Carmesin, M. Schowalter, M. Lorke, D. Mourad, T. Grieb, K. Müller-Caspary, M. Yacob, J. P. Reithmaier, M. Benyoucef, A. Rosenauer, F. Jahnke, *Phys. Rev. B* **2017**, *96*, 235309.
[24] I. A. Yugova, M. M. Glazov, E. L. Ivchenko, A. L. Efros, *Phys. Rev. B* **2009**, *80*, 104436.
[25] V. V. Belykh, A. Greilich, D. R. Yakovlev, M. Yacob, J. P. Reithmaier, M. Benyoucef, M. Bayer, *Phys. Rev. B* **2015**, *92*, 165307.
[26] A. Bracker, M. Scheibner, M. Doty, E. Stinaff, I. Ponomarev, J. Kim, L. Whitman, T. Reinecke, D. Gammon, *Appl. Phys. Lett.* **2007**, *89*, 233110.
[27] C. Testelin, F. Bernardot, B. Eble, M. Chamarro, *Phys. Rev. B* **2009**, *79*, 195440.
[28] I. A. Merkulov, A. L. Efros, M. Rosen, *Phys. Rev. B* **2002**, *65*, 205309.
[29] W. Liu, S. Sanwlani, R. Hazbun, J. Kolodzey, A. S. Bracker, D. Gammon, M. F. Doty, *Phys. Rev. B* **2011**, *84*, 121304.
[30] C. E. Pryor, M. E. Flatté, *Phys. Rev. Lett.* **2006**, *96*, 026804.
[31] I. A. Yugova, A. Greilich, E. A. Zhukov, D. R. Yakovlev, M. Bayer, D. Reuter, A. D. Wieck, *Phys. Rev. B* **2007**, *75*, 195325.
[32] L. M. Roth, B. Lax, S. Zwerdling, *Phys. Rev.* **1959**, *114*, 90.
[33] C. Gradl, R. Winkler, M. Kempf, J. Holler, D. Schuh, D. Bougeard, A. Hernández-Mnguez, K. Biermann, P. V. Santos, C. Schüller, T. Korn, *Phys. Rev. X* **2018**, *8* 021068.
[34] F. Heisterkamp, E. A. Zhukov, A. Greilich, D. R. Yakovlev, V. L. Korenev, A. Pawlis, M. Bayer, *Phys. Rev. B* **2015**, *91*, 235432.
[35] E. A. Zhukov, E. Kirstein, D. S. Smirnov, D. R. Yakovlev, M. M. Glazov, D. Reuter, A. D. Wieck, M. Bayer, A. Greilich, *Phys. Rev. B* **2018**, *98*, 121304.
[36] D. S. Smirnov, E. A. Zhukov, E. Kirstein, D. R. Yakovlev, D. Reuter, A. D. Wieck, M. Bayer, A. Greilich, M. M. Glazov, *Phys. Rev. B* **2018**, *98*, 125306.
[37] A. V. Khaetskii, Y. V. Nazarov, *Phys. Rev. B* **2001**, *64*, 125316.
[38] M. Trif, P. Simon, D. Loss, *Phys. Rev. Lett.* **2009**, *103*, 106601.
[39] A. Greilich, D. R. Yakovlev, A. Shabaev, A. L. Efros, I. A. Yugova, R. Oulton, V. Stavarache, D. Reuter, A. Wieck, M. Bayer, *Science* **2006**, *313*, 341.
[40] E. Evers, V. V. Belykh, N. E. Kopteva, I. A. Yugova, A. Greilich, D. R. Yakovlev, D. Reuter, A. D. Wieck, M. Bayer, *Phys. Rev. B* **2018**, *98* 075309.
[41] E. Kirstein, N. E. Kopteva, D. R. Yakovlev, E. A. Zhukov, E. V. Kolobkova, M. S. Kuznetsova, V. V. Belykh, I. A. Yugova, M. M. Glazov, M. Bayer, A. Greilich, *Nat. Commun.* **2023**, *14*, 699.
[42] I. A. Yugova, M. M. Glazov, D. R. Yakovlev, A. A. Sokolova, M. Bayer, *Phys. Rev. B* **2012**, *85*, 125304.
[43] D. Heiss, S. Schaeck, H. Huebl, M. Bichler, G. Abstreiter, J. J. Finley, D. V. Bulaev, D. Loss, *Phys. Rev. B* **2007**, *76*, 241306.
[44] C. Lü, J. L. Cheng, M. W. Wu, *Phys. Rev. B* **2005**, *71*, 075308.
[45] L. M. Woods, T. L. Reinecke, Y. Lyanda-Geller, *Phys. Rev. B* **2002**, *66*, 161318.
[46] D. V. Bulaev, D. Loss, *Phys. Rev. Lett.* **2005**, *95*, 076805.
[47] F. Fras, B. Eble, P. Desfonds, F. Bernardot, C. Testelin, M. Chamarro, A. Miard, A. Lematre, *Phys. Rev. B* **2012**, *86*, 045306.
[48] L. Huthmacher, R. Stockill, E. Clarke, M. Hugues, C. Le Gall, M. Atatüre, *Phys. Rev. B* **2018**, *97*, 241413.
[49] S. Varwig, A. René, A. Greilich, D. R. Yakovlev, D. Reuter, A. D. Wieck, M. Bayer, *Phys. Rev. B* **2013**, *87*, 115307.
[50] A. G. Aronov, G. L. Bir, G. E. Pikus, *Sov. Phys. JETP* **1975**, *42*, 705.
[51] S. Varwig, E. Evers, A. Greilich, D. R. Yakovlev, D. Reuter, A. D. Wieck, M. Bayer, *Phys. Rev. B* **2014**, *90*, 121306.
[52] G. Wüst, M. Munsch, F. Maier, A. V. Kuhlmann, A. Ludwig, A. D. Wieck, D. Loss, M. Poggio, R. J. Warburton, *Nat. Nanotechnol.* **2016**, *11*, 885.
[53] P. Millington-Hotze, S. Manna, S. F. Covre da Silva, A. Rastelli, E. A. Chekhovich, *Nat. Commun.* **2023**, *14*, 2677.
[54] J. H. Bodey, R. Stockill, E. V. Denning, D. A. Gangloff, G. Éthier-Majcher, D. M. Jackson, E. Clarke, M. Hugues, C. L. Gall, M. Atatüre, *npj Quantum Inf.* **2019**, *5*, 95.
[55] D. A. Gangloff, G. Éthier Majcher, C. Lang, E. V. Denning, J. H. Bodey, D. M. Jackson, E. Clarke, M. Hugues, C. L. Gall, M. Atatüre, *Science* **2019**, *364*, 62.
[56] M. H. Appel, A. Ghorbal, N. Shofer, L. Zaporski, S. Manna, S. F. C. da Silva, U. Haeusler, C. L. Gall, A. Rastelli, D. A. Gangloff, M. Atatüre, Many-body quantum register for a spin qubit, https://arxiv.org/abs/2404.19680 (accessed: April 2024).
[57] J. Michl, G. Peniakov, A. Pfenning, J. Hilska, A. Chellu, A. Bader, M. Guina, S. Höfling, T. Hakkarainen, T. Huber-Loyola, *Adv. Quantum Technol.* **2023**, *6*, 2300180.